

Multi-epoch high-resolution spectroscopy of SN 2011fe[★]

Linking the progenitor to its environment

F. Patat¹, M. A. Cordiner², N. L. J. Cox³, R. I. Anderson⁴, A. Harutyunyan⁵, R. Kotak⁶, L. Palaversa⁴, V. Stanishev⁷,
L. Tomasella⁸, S. Benetti⁹, A. Goobar¹⁰, A. Pastorello⁹, and J. Sollerman¹⁰

- ¹ European Organization for Astronomical Research in the Southern Hemisphere (ESO), Karl-Schwarzschild-Str. 2, 85748, Garching b. München, Germany e-mail: fpatat@eso.org
² Astrochemistry Laboratory and the Goddard Center for Astrobiology, Mailstop 691, NASA Goddard Space Flight Center, 8800 Greenbelt Road, Greenbelt, MD 20770, USA
³ Instituut voor Sterrenkunde, K.U. Leuven, Celestijnenlaan 200 D, B-3001 Leuven, Belgium
⁴ Observatoire de Genève, Université de Genève, 51 Ch. des Maillettes, CH-1290 Sauverny, Switzerland
⁵ Fundación Galileo Galilei - Telescopio Nazionale Galileo, Rambla José Ana Fernández Pérez 7, 38712 Breña Baja, TF - Spain
⁶ Astrophysics Research Center, School of Mathematics and Physics, Queens University Belfast, Belfast, BT7 1NN, UK
⁷ CENTRA - Centro Multidisciplinar de Astrofísica, Instituto Superior Técnico, Av. Rovisco Pais 1, 1049-001 Lisbon, Portugal
⁸ INAF, Osservatorio Astronomico di Padova, via dell'Osservatorio 8, I-36012, Asiago (VI), Italy
⁹ INAF, Osservatorio Astronomico di Padova, v. Osservatorio n.5, I-35122, Padua, Italy
¹⁰ Albanova University Center, Department of Physics, Stockholm University Roslagstullsbacken 21, 106 91 Stockholm, Sweden

Received November, 2011; accepted...

ABSTRACT

Context. The nearby Type Ia SN 2011fe has provided an unprecedented opportunity to derive some of the properties of the progenitor system, which is one of the key open problems in the supernova (SN) field.

Aims. This study attempts to establish a link between the reasonably well known nature of the progenitor and its surrounding environment. This is done with the aim of enabling the identification of similar systems in the vast majority of the cases, when distance and epoch of discovery do not allow a direct approach.

Methods. To study the circumstellar environment of SN 2011fe we have obtained high-resolution spectroscopy of SN 2011fe on 12 epochs, from 8 to 86 days after the estimated date of explosion, targeting in particular at the time evolution of Ca II and Na I.

Results. Three main absorption systems are identified from Ca II and Na I, one associated to the Milky Way, one probably arising within a high-velocity cloud, and one most likely associated to the halo of M101. The Galactic and host galaxy reddening, deduced from the integrated equivalent widths (EW) of the Na I lines are $E_{B-V}=0.011\pm0.002$ and $E_{B-V}=0.014\pm0.002$ mag, respectively. The host galaxy absorption is dominated by a component detected at the same velocity measured from the 21-cm H I line at the projected SN position (~ 180 km s⁻¹). During the ~ 3 months covered by our observations, its EW changed by 15.6 ± 6.5 mÅ. This small variation is shown to be compatible with the geometric effects produced by the rapid SN photosphere expansion coupled to the patchy fractal structure of the ISM. The observed behavior is fully consistent with ISM properties similar to those derived for our own Galaxy, with evidences for structures on scales ≤ 100 AU.

Conclusions. SN 2011fe appears to be surrounded by a "clean" environment. The lack of blue-shifted, time-variant absorption features is fully consistent with the progenitor being a binary system with a main-sequence, or even another degenerate star.

Key words. supernovae: general - supernovae: individual: SN 2011fe - ISM: dust, extinction

1. Introduction

Since the introduction of the accreting White Dwarf (WD) scenario (Wheeler & Iben 1973), the question mark about the nature of the progenitor systems of Type Ia Supernovae (hereafter

SN Ia) has been growing bigger and bigger (see Patat 2011 for a general review on the subject). One of the most beaten tracks to obtain information on the progenitor system (and more specifically on the nature of the donor star) has been the search for imprints of circumstellar material (CSM) lost by the system prior to the explosion. Notwithstanding the extensive attempts undertaken to detect such material, as of today no signs of it have been found in the form of optical (Lundqvist 2003, 2005;

[★] Based on observations collected at the Mercator telescope, Telescopio Nazionale Galileo, Nordic Optical Telescope at Roque de los Muchachos, La Palma (Spain), and at the 1.82 m Copernico telescope on Mt. Ekar (Asiago, Italy).

Table 1. Log of the observations

Date	UT (start)	JD (start)	Phase (days) ^(*)	Epoch (days) ^(**)	Airmass (start)	Exposure (seconds)	Instrument	Hel. Correction (km s ⁻¹)
31-08-2011	20:39	2455805.357	-11	8.2	1.64	1800	FIES	-4.19
03-09-2011	20:20	2455808.344	-8	11.2	1.52	3600	SARG	-3.46
07-09-2011	20:20	2455812.340	-4	15.1	1.58	1800	HERMES	-2.47
13-09-2011	19:23	2455818.308	+2	21.1	1.60	4200	AES	-0.94
13-09-2011	20:16	2455818.342	+2	21.1	1.72	1350	HERMES	-0.96
14-09-2011	18:57	2455819.290	+3	22.1	1.50	3600	AES	-0.69
21-09-2011	18:59	2455826.291	+10	29.1	1.63	5400	AES	+1.09
22-09-2011	18:40	2455827.278	+11	30.1	1.56	9000	AES	+1.35
29-09-2011	20:47	2455834.363	+18	37.2	2.63	2700	FIES	+3.10
18-10-2011	17:54	2455853.246	+37	56.1	1.84	7200	AES	+7.68
15-11-2011	16:52	2455881.203	+65	84.0	2.80	4800	AES	+12.86
18-11-2011	01:28	2455883.561	+67	86.4	2.65	12600	AES	+13.52
18-11-2011	05:05	2455883.710	+67	86.5	2.92	4800	SARG	+13.55

(*) Phases from *V* maximum were computed assuming a typical rise time of 19 days.

(**) Epochs are computed from the estimated explosion time (JD=2455797.196; Nugent et al. 2011c).

Mattila et al. 2005), radio (Panagia et al. 2006, Chomiuk et al. 2011), and UV/X-Ray emission (Immler et al. 2006).

Independent information on the binary system can be obtained studying the effects the explosion has on the companion star. So far two possibilities have been explored: the collision of the SN ejecta with the companion star surface, and the stripping of the companion's envelope. While the former is expected to re-heat part of the SN ejecta causing a luminosity excess in the very early epochs (Kasen 2010), the latter is supposed to entrain some of the companion atmospheric material, which should eventually become visible in the form of emission lines at late epochs (see e.g. Marietta, Burrows & Fryxell 2000, and references therein). So far, no evidences of either phenomena have been found (Hayden et al. 2010; Bianco et al. 2011; Leonard 2007).

These facts constitute a considerable body of evidence in favor of SN Ia progenitor systems where the companion star is either a MS star, or even another degenerate body. However, it is only with the very recent study of SN 2011fe that this was directly demonstrated with a high level of confidence. SN 2011fe (PTF11kly) was discovered by the Palomar Transient Factory on August 24 UT in the outskirts of the nearby (~ 6 Mpc), face-on, SAB(rs)cd galaxy M101 (NGC 5457), and immediately classified as a very early Type Ia (Nugent et al. 2011a, 2011b). The SN was not detected (down to mag 20.6) on an image taken on August 23, implying the object was caught within one day after the explosion.

Based on pre-explosion HST images, Li et al. (2011) could place for the first time a direct and stringent limit on the companion's luminosity. This rules out a red-giant donor star, and hence a symbiotic system as the progenitor for this particular event. The observations presented by Li et al. (2011) exclude the He-star channel only partially, while a system with a MS-star transferring mass via Roche lobe overflow is still consistent with the data, as is a double-degenerate configuration. The lack of an early shock (Nugent et al. 2011c) goes along the same lines, ruling out companion stars with extended atmospheres.

Thanks to the very early detection, Nugent et al. (2011c) could put a stringent upper limit to the exploding star radius ($\leq 0.1 R_{\odot}$), hence providing for the first time a direct evidence that the progenitor is indeed a compact star (see also Brown et al. 2011). Although a carbon-burning MS star cannot not be excluded, a C-O WD is the most favored candidate. The range of allowed objects was further narrowed down by Bloom et al. (2011), who derived a more stringent upper limit for the progenitor radius ($0.02 R_{\odot}$), and concluded that the exploding star must indeed be a WD (for independent considerations on the progenitor's nature, see also Liu et al. 2011). Bloom et al. (2011) also place an upper limit to the radius of the companion ($0.1 R_{\odot}$), which excludes Roche-lobe overflowing giants and MS stars. Finally, prompt radio and X-ray observations placed the most stringent limit ever on the mass loss rate for a SN Ia: $dM/dt \leq 10^{-8}$ ($w/100 \text{ km s}^{-1}$) $M_{\odot} \text{ yr}^{-1}$ (Horesh et al. 2011).

All these facts give a very consistent view on the progenitor system of SN 2011fe, which is very plausibly identified as a C-O WD accreting material from a MS star (Li et al. 2011; Brown et al. 2011; Nugent et al. 2011c; Bloom et al. 2011). This is a major break-through in the field. Having studied an object whose progenitor system is reasonably well known, we can now ask ourselves a new question. Would we recognize similar systems in other SN Ia, whose distance and discovery time do not allow the close scrutiny that was possible for SN 2011fe? The key issue here is that one needs to consider the largest possible number of observables, because, for instance, similar spectra and light curves may come from different channels.

In this article we focus on the properties of the circumstellar environment, whose study has led to promising results in the last years (Patat et al. 2007a; Simon et al. 2009; Sternberg et al. 2011). For this purpose, and following the previous studies, we have obtained multi-epoch, high-resolution, optical spectroscopy of SN 2011fe covering the first three months of its evolution.

The paper, reporting the results of this campaign, is structured as follows. In Sect. 2 we give an account of the observations and data reduction. Sect. 3 recaps the detection of narrow

Table 2. Instrumental setups

ID	Site	Telescope	Res. power	Disp. (Å/pixel)	Range (Å)
AES	Asiago	1.8-m	18 000	0.126	3800-7500
FIES	La Palma	2.6-m	48 000	0.036	3650-7350
HERMES	La Palma	1.2-m	82 000	0.016	3770-9000
SARG	La Palma	3.5-m	66 000	0.021	4600-6150

absorption features, whereas Sect. 4 discusses the implications on the extinction suffered by the SN. In Sect. 5 we illustrate the properties of the intervening gas as derived from Voigt profile fittings, and we study their behavior as a function of time. The modest time evolution is then analyzed in Sect. 6, in the context of the small-scale structure of the inter-stellar medium. The results of this study in connection to the progenitor's nature are finally discussed in Sect. 7, which also summarizes our conclusions.

2. Observations and data reduction

We obtained high-resolution spectroscopy of SN 2011fe on 12 epochs, ranging from 8 to 86 days after the estimated date of explosion (JD=2455797.2; Nugent et al. 2011c). The observing log is presented in Table 1, which includes exposure times, phase from maximum light, epoch from explosion, airmass, and heliocentric correction. Phases are only indicative, and were computed assuming a typical SN Ia rise time of 19 days. The observations were carried out with four different instrumental setups. These are summarized in Table 2, and detailed in the next subsections.

2.1. Asiago Echelle Spectrograph

Seven spectra of SN 2011fe were obtained with the REOSC Asiago Echelle Spectrograph (hereafter AES) attached to the 1.82 m telescope on Mt. Ekar (Asiago, Italy). The spectrograph is equipped with an E2V CCD42-40 AIMO, back illuminated detector (2048×2048 pixel, 13.5 μm in size). A 2'' slit was used, with a fixed east-west orientation, yielding a resolving power $R = \lambda/\Delta\lambda \sim 18\,000$. The wavelength range covered by the spectra is 3780-7620 Å. The data reduction was performed with tasks within the IRAF¹ ECHELLE package following the standard procedures. All images were first over-scan corrected and trimmed. A normalized flat-field image was then derived from observations of a halogen lamp and used to flat field the science exposures. Next, each spectral order was traced and the spectra were extracted with the optimal extraction algorithm of Horne (1986), simultaneously subtracting the scattered light. The transformation from pixels to wavelength was derived from observations of a Thorium-Argon arc-lamp.

¹ IRAF is distributed by the National Optical Astronomy Observatories, which are operated by the Association of Universities for Research in Astronomy, under contract with the National Science Foundation.

2.2. FIES

Two spectra (Aug 31 and Sep 29, 2011) were obtained with the fiber-fed (1.3'') echelle spectrograph (FIES²) mounted at the Nordic Optical Telescope (NOT) on La Palma (Spain). We used the medium-resolution fiber, that provides a resolving power $R \sim 48\,000$, and continuous spectral coverage from 3700 to 7300 Å in a single exposure. Data were reduced using standard IRAF tasks, as outlined in the previous section.

2.3. HERMES

Two spectra (Sep 7 and 13, 2011) were obtained with the High Efficiency and Resolution Mercator Echelle Spectrograph (HERMES; Raskin et al. 2011), mounted on the Mercator 1.2 m telescope in La Palma. HERMES is a high-resolution fiber-fed (2.5'') echelle spectrograph offering spectral resolution of $R \sim 80\,000$, and full spectral coverage from 3770 to 9000 Å in a single exposure. Data were processed with an automated data reduction pipeline that includes bias correction from the prescan region on the CCD, flat-field correction via Halogen lamps, wavelength calibration through Th-Ar reference spectra, cosmic clipping, and background modelization.

2.4. SARG

Two spectra (Sep 3, and Nov 18, 2011) were obtained with the Spetrografo Alta Risoluzione Galileo (SARG; Gratton et al. 2001), mounted at the 3.5 m Telescopio Nazionale Galileo (TNG) in La Palma. SARG is a cross-dispersed echelle spectrograph which provides spectral resolution ranging from $R=29\,000$ up to $R=164,000$. For our observations we used the cross-disperser #3 grism, a GG455 order sorting filter, and slit #2 (0.8''×5.3''). This setup yields $R \sim 66,000$ and a wavelength range 4600-6150 Å. The data reduction was performed using standard IRAF tasks, as outlined in Sect. 2.1.

2.5. Removal of telluric features

Although the spectral region of Ca II H&K is free of telluric absorption features, this is not the case for Na I D, and especially K I $\lambda 7665$ and $\lambda 7699$. Because the observations were conducted mostly at relatively high airmasses (see Table 1) these are quite severely disturbed by water bands.

The removal of telluric absorption features is usually performed using spectra of bright stars obtained with the same instrumental setup and similar airmass as for the scientific target. In this paper we adopted a different approach, using an atmospheric transmission model (see for instance Stevenson 1994; Seifahrt et al. 2010). The advantages over a direct observation are: a) the absence of intrinsic photospheric features, b) the absence of interstellar features (chiefly Na I D lines), c) the infinite signal-to-noise, and d) the exact wavelength scale. The latter provides an absolute reference to which the observed spectra can be corrected via cross-correlation techniques (see below).

² <http://www.not.iac.es/instruments/fies/>

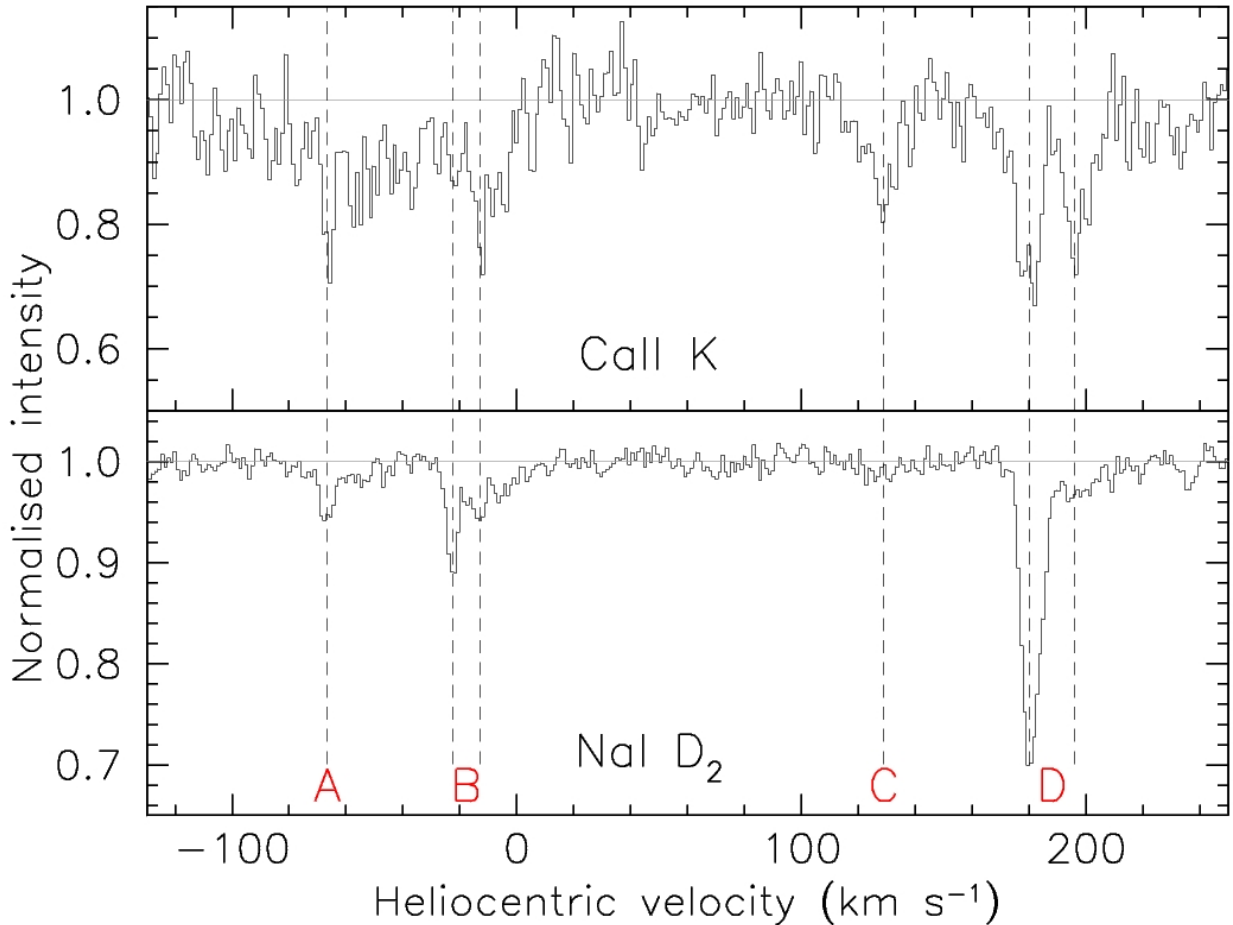


Fig. 2. Narrow absorption components towards SN 2011fe for Ca II K (upper panel; day 21) and Na I D₂ (lower panel; day 11.2). Main absorption features are marked by vertical dashed lines.

In this work we adopted the Line By Line Radiation Transfer Model (LBLRTM; Clough et al. 2005). This code is based on the HITRAN database (Rothman et al. 2009). It has been validated against real spectra from the UV to the sub-millimeter, and is widely used for the retrieval of atmospheric constituents³. LBLRTM solves the radiative transfer using an input atmospheric profile, which contains the height profiles for temperature, pressure, and chemical composition. For our purposes we have adopted the standard LBLRTM equatorial profile.

After computing the synthetic model in the regions of interest and for the given airmass, this is convolved with the instrumental profile and the wavelength correction is computed via cross-correlation. The absence of intrinsic narrow absorptions in the SN spectrum and the weakness of the interstellar features in the Na I and K I regions (see below) make the correlation function peak very well defined. The wavelength solutions for FIES, HERMES and SARG spectra were all found to match the model wavelength with a maximum deviation of 130 m s⁻¹, that is more than 5 times smaller than the pixel size. Therefore, no wavelength correction was applied to these data. In the case of the AES spectra, maximum deviations of 6.6 km s⁻¹ (about

one pixel) were found, and the spectra were corrected accordingly. The final wavelength accuracy is ~ 0.1 km s⁻¹ for FIES, HERMES and SARG data, while this is ~ 0.3 km s⁻¹ for the AES spectra.

An example of telluric correction is presented in Fig. 1 for the SARG spectrum. All telluric features are removed at the level of a few percent, which is comparable to (or better than) the continuum RMS noise of all spectra presented in this paper.

As a for the sky background subtraction, we note that in some spectra the terrestrial Na I D emission components (both natural and artificial) are not completely removed. Because of the wavelength shift of most features, this problem does affect only a Galactic absorption close to null restframe velocity (see Sect. 3), whose profile (and thus equivalent width) is most likely affected by the incomplete sky subtraction.

3. Narrow absorption features in SN 2011fe

3.1. Ca II H&K and Na I D

A number of Ca II H,K and Na I D components are detected at different velocities, as shown in Fig. 2, which presents the highest resolution spectra available for the two wavelength ranges

³ See <http://rtweb.aer.com/lblrtm.html>

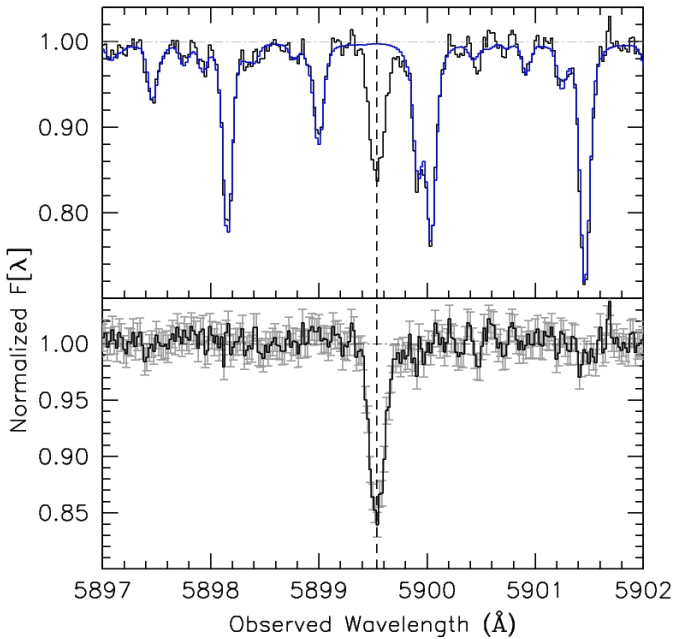


Fig. 1. Example of telluric features removal for the SARG spectrum in the region of Na I D₂. Upper panel: observed data (black line) and best fit LBLRTM model (blue line). Lower panel: telluric-corrected spectrum. The dashed vertical line marks the position of Na I D₂ ($v_{hel} \sim 180 \text{ km s}^{-1}$). The signal-to-noise ratio on the continuum is about 100 (the error-bars indicate the estimated RMS noise).

(obtained with HERMES and SARG, respectively; see Tables 1 and 2).

Two main Galactic absorption systems are detected around -70 and -20 km s^{-1} (marked as A and B in Fig. 2), with weaker and diffuse absorptions possibly present at intermediate velocities (see the Ca II profile). A third system is clearly detected at about $+130 \text{ km s}^{-1}$ (C). The recession velocity of M101 is $241 \pm 2 \text{ km s}^{-1}$ (de Vaucouleurs et al. 1991), and therefore this component may be generated within a high-velocity cloud (HVC) belonging either to the Milky Way or to the host galaxy. The radial velocity derived from 21-cm line observations at the projected SN site is about 180 km s^{-1} (Bosma, Goss & Allen 1981; their Fig. 1). This makes the association to M101 more plausible, although not certain (see also Sect. 5). Finally, we detect an absorption system with two main components at about 180 and 195 km s^{-1} (D). These velocities are fully consistent with the radial velocity field at the projected SN location (Bosma et al. 1981). This strongly suggests that the corresponding absorptions arise in M101. All features are detected in both H and K lines, while system C is not detected in Na I. The component close to 195 km s^{-1} is clearly detected in Na I only in the highest signal-to-noise spectrum (SARG, day 11) with a total equivalent width $EW=7 \pm 2 \text{ mÅ}$, while it is only marginally detected in all other spectra.

Nugent et al. (2011c) report the detection of one single absorption feature ($EW=45 \pm 9 \text{ mÅ}$), which they identify as Na I D₂ at $v=194 \pm 1 \text{ km s}^{-1}$. Although the weighted average EW

we derive from our data ($EW(\text{Na I D}_2)=47 \pm 1 \text{ mÅ}$, $EW(\text{Na I D}_1)=27 \pm 1 \text{ mÅ}$; see Sect. 5.1) is consistent with that reported by Nugent et al., velocity discrepancy is statistically very significant ($\sim 14 \text{ km s}^{-1}$), and cannot be explained in terms of the quoted errors. Once applying the heliocentric corrections listed in Table 1 to the different spectra, the velocities deduced for the Na I D components all agree to within a few 0.1 km s^{-1} . The average heliocentric velocity deduced from the best fit profile of the most intense host galaxy component (see Sect. 5) is $179.6 \pm 0.2 \text{ km s}^{-1}$. Given the very consistent results we obtain from different setups and epochs, we believe our result is correct to within the reported errors.

3.2. Other absorptions

A careful inspection of the telluric-corrected spectra covering the relevant wavelength range shows no trace of the two typical K I lines at 7665 and 7699 Å , both for the Galaxy and for M101 (at the velocities derived for the Ca II and Na I features. See previous section). For the host galaxy the $5\text{-}\sigma$ detection limit derived from the HERMES spectrum taken on day 15 is $EW(\text{K I } \lambda 7699) < 5 \text{ mÅ}$. The K I $\lambda 7665$ is severely affected by a telluric absorption, and so the upper limit estimate for this line is more problematic. However, the two lines have very similar strengths, and so the limit derived above applies to both of them. Similar considerations apply to the non-detection of Ti II, Ca I, CH and CH+.

Finally, none of the known strong Diffuse Interstellar Bands (DIBs; 5780 , 5797 , 6284 , 6379 , 6613 ; Herbig 1995) are detected.

4. Reddening

The galactic Na I D components are very weak (see Fig. 2), indicating that SN 2011fe suffers a very low Galactic reddening. The integrated $EW(\text{Na I D}_1)$ derived from our highest signal-to-noise spectrum (SARG, day 11) for the Galactic components (systems A and B in Fig. 2) is $38 \pm 5 \text{ mÅ}$. Applying the relation inferred by Munari & Zwitter (1997) for Galactic reddening, we get $E_{B-V}=0.011 \pm 0.002 \text{ mag}$, which is consistent with the expected Galactic extinction along the line of sight to M101 ($E_{B-V}=0.009 \text{ mag}$; Schlegel, Finkbeiner & Davies 1998). According to the Munari & Zwitter relation, the expected EW for the K I $\lambda 7699$ is $\sim 4 \text{ mÅ}$, which is fully consistent with the lack of K I detection in our spectra.

As shown in the previous section, we detect two features most probably associated to the host galaxy, at ~ 180 and $\sim 200 \text{ km s}^{-1}$, with the latter contributing only marginally to the total Na I column density. The integrated D₂ EW measured on the SARG spectrum (day 11) is $47 \pm 2 \text{ mÅ}$ ($EW(\text{Na I D}_1)=25 \pm 1 \text{ mÅ}$). Applying the Munari & Zwitter relation, this turns into $E_{B-V}=0.014 \pm 0.002 \text{ mag}$ ($A_V=0.04 \text{ mag}$), in agreement with the value derived by Nugent et al. (2011c) using the same method.

Independent constraints on the reddening can be placed studying the DIBs (see for instance Sollerman et al. 2005, Cox & Patat 2008). As it turns out, these are much less stringent than those derived from the sodium lines, and we mention them

Table 3. Na I and Ca II interstellar cloud model parameters

Weighted Average			Day 8	Day 11	Day 15	Day 21	Day 37
v	b	N	N	N	N	N	N
Na I							
-67.2	2.1	10.52 ^{+0.08} _{-0.11}	10.52 ^{+0.18} _{-0.26}	10.53 ^{+0.06} _{-0.07}	10.36 ^{+0.16} _{-0.19}	10.62 ^{+0.08} _{-0.10}	10.50 ^{+0.18} _{-0.25}
-23.3	3.0	10.74 ^{+0.07} _{-0.08}	10.70 ^{+0.13} _{-0.16}	10.80 ^{+0.04} _{-0.04}	10.80 ^{+0.07} _{-0.08}	10.73 ^{+0.06} _{-0.08}	10.60 ^{+0.16} _{-0.20}
-12.6	3.4	10.55 ^{+0.11} _{-0.11}	10.18 ^{+0.35} _{-0.79}	10.64 ^{+0.06} _{-0.06}	10.27 ^{+0.20} _{-0.29}	10.66 ^{+0.08} _{-0.09}	10.80 ^{+0.11} _{-0.14}
179.6	3.8	11.44 ^{+0.02} _{-0.02}	11.43 ^{+0.03} _{-0.04}	11.43 ^{+0.01} _{-0.01}	11.43 ^{+0.02} _{-0.02}	11.44 ^{+0.02} _{-0.02}	11.51 ^{+0.03} _{-0.03}
193.6	6.4	10.57 ^{+0.12} _{-0.16}	10.56 ^{+0.20} _{-0.29}	10.46 ^{+0.09} _{-0.13}	10.50 ^{+0.16} _{-0.18}	10.64 ^{+0.11} _{-0.11}	10.42 ^{+0.26} _{-0.46}
Ca II							
-66.4	0.7	11.10 ^{+0.17} _{-0.20}	11.05 ^{+0.34} _{-0.69}		11.15 ^{+0.16} _{-0.21}	11.07 ^{+0.18} _{-0.24}	
-65.7	32.0	11.90 ^{+0.07} _{-0.07}	12.00 ^{+0.08} _{-0.07}		11.85 ^{+0.10} _{-0.10}	11.89 ^{+0.09} _{-0.10}	
-37.5	1.0	10.91 ^{+0.20} _{-0.24}	< 11.10		10.91 ^{+0.20} _{-0.30}	10.97 ^{+0.18} _{-0.25}	
-23.5	3.1	11.04 ^{+0.17} _{-0.24}	11.00 ^{+0.23} _{-0.35}		11.03 ^{+0.19} _{-0.26}	11.03 ^{+0.17} _{-0.26}	
-9.4	7.3	11.63 ^{+0.06} _{-0.06}	11.72 ^{+0.07} _{-0.09}		11.61 ^{+0.08} _{-0.08}	11.58 ^{+0.08} _{-0.10}	
127.8	6.2	11.54 ^{+0.07} _{-0.07}	11.61 ^{+0.09} _{-0.10}		11.55 ^{+0.07} _{-0.10}	11.46 ^{+0.09} _{-0.13}	
179.2	5.5	11.82 ^{+0.04} _{-0.04}	11.89 ^{+0.05} _{-0.07}		11.80 ^{+0.05} _{-0.06}	11.78 ^{+0.05} _{-0.05}	
197.0	6.7	11.58 ^{+0.07} _{-0.08}	11.64 ^{+0.08} _{-0.09}		11.50 ^{+0.09} _{-0.11}	11.60 ^{+0.09} _{-0.09}	
218.5	3.5	10.89 ^{+0.21} _{-0.31}	< 11.10		10.99 ^{+0.18} _{-0.31}	10.82 ^{+0.26} _{-0.50}	

here only for the sake of completeness. Assuming a standard relation between DIB strength and E_{B-V} (e.g. Luna et al. 2008; $EW(6613)/E_{B-V}=310 \text{ m\AA}$), and based on the lack of DIB detection (see previous section) gives an upper limit on the M101 reddening of 0.4 mag. A similar assessment for the 5780 DIB ($EW(5780)/E_{B-V}=460 \text{ m\AA}$) gives $E(B-V) \leq 0.43$ mag. Due to the intrinsic weakness of other DIBs, the upper limits on their EW derived from our spectra give even less stringent constraints. For example, the non-detection of the 6379 DIB yields $E_{B-V} < 0.65$ mag ($EW(6379)/E_{B-V}=88 \text{ m\AA}$; Luna et al. 2008).

5. Narrow absorption line modeling

In order to derive interstellar cloud velocities, Doppler widths, and column densities we modeled the best resolution and signal-to-noise spectra using the `VARD` routine (Howarth et al. 2002). Saturation effects were implicitly taken into account fitting simultaneously lines of the same species (Na I D₁ and D₂; Ca II H and K). The results for the FIES, HERMES and SARG (first epoch only) spectra are shown in Figs. 3 and 4 for Na I and Ca II. The Na I spectra require 5 components for a good fit, whereas 9 components were required for Ca II. Error estimates were derived using Monte Carlo noise replication. The models were re-fit to 1000 replicated data-sets, each with Gaussian noise of RMS equal to that of the continuum added. The $\pm 68\%$ ranges in the resulting data give rigorous 1σ errors on each parameter. Results are given in Table 3 for each epoch, as well as the results of a weighted-average fit to all epochs, in which the fitted data points were weighted by the continuum signal-to-noise ratio of the respective spectra. The data show no evidence for statistically significant variations in cloud component velocities or Doppler b parameters between epochs (see below), so the v and b values were held fixed at the weighted-average fit values and only the N values were allowed to vary

for each epoch. Column densities (cm^{-2}) are given as base-ten logarithms. The units of v and b are km s^{-1} .

The analysis of Milky Way interstellar gas is beyond the scope of this paper. Here we mention that for the most marked Galactic feature (-23 km s^{-1}), the $N(\text{Na I})/N(\text{Ca II})$ ratio is ~ 0.50 , which is typical of galactic halos (Hobbs 1978; Crawford 1992; Bertin et al. 1993). Sembach & Danks (1994) measured a mean Galactic Halo $N(\text{Na I})/N(\text{Ca II}) \sim 0.5$.

Interestingly, the $N(\text{Na I})/N(\text{Ca II})$ ratio for the main feature in M101 ($+180 \text{ km s}^{-1}$) is ~ 0.43 , indicating that it may as well originate in the halo of the host galaxy (see also King et al. 1995 for the case of SN 1994D). The really deviant case is the one of the component at $\sim 128 \text{ km s}^{-1}$, which is clearly detected in Ca II but not in Na I. The upper limit to the Na I column density deduced from the high-signal to noise SARG spectrum (day 11) is $1.5 \times 10^{10} \text{ cm}^{-2}$, which yields $N(\text{Na I})/N(\text{Ca II}) \leq 0.04$. Such low values are rarely observed, and indicate a mild depletion of calcium onto dust grains. A similar case was observed for one high velocity component along the line of sight to SN 2000cx, where Ca II was detected while Na I was not (Patat et al. 2007b). The corresponding ratio was $N(\text{Na I})/N(\text{Ca II}) \leq 0.1$. Finally, King et al. (1995) found $N(\text{Na I})/N(\text{Ca II}) = 0.1-0.3$ for the high-velocity clouds observed along the line of sight to SN 1994D. Low ratios are, in general, typical of high velocity gas (Siluk & Silk 1974). The small value we derived for the component at $\sim 180 \text{ km s}^{-1}$ is similar to those observed in intermediate- and high-velocity clouds by Molaro et al. (1993), who concluded that such clouds may contain very little dust, with calcium and sodium mainly in gaseous form (see also the properties measured by Cox et al. 2007 towards LMC sight-lines). For these reasons it is reasonable to conclude that absorption system C (see Fig. 2) arises in a HVC.

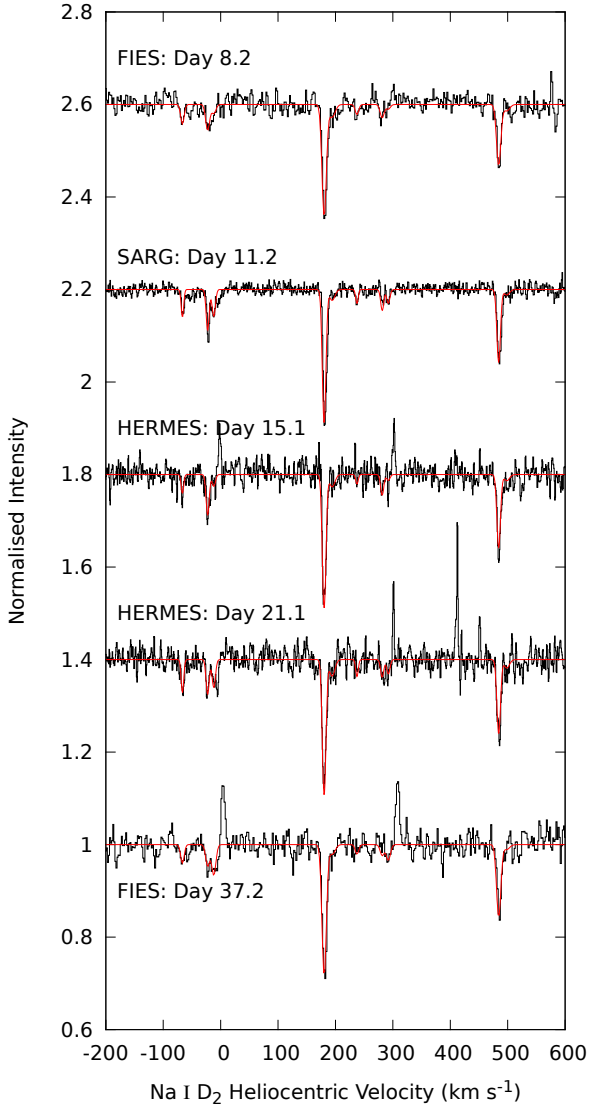


Fig. 3. Na I D spectra for each epoch (black histograms), with best-fit models overlaid (red curves). Spectra have been normalised and offset vertically for display. Heliocentric velocity scale is given with respect to the Na D₂ line rest wavelength. The spurious emissions observed in some spectra around 0 and 300 km s⁻¹ are residuals of the sky subtraction (see Sect. 2).

5.1. Time evolution

The derived cloud parameters show some marginal evidence for time variability. The only possibly significant variation is seen for the host galaxy Na I component at ~ 180 km s⁻¹. While the logarithmic column density derived for this absorption is 11.44 ± 0.02 on days 8, 11, 15 and 21, on day 37 this grows to 11.52 ± 0.03 , which indicates a variation at the 3-sigma level. One may be tempted to attribute this fluctuation to the different instrumental setups. However, a direct comparison of the two spectra taken on days 8 and 37 (both obtained with FIES and the same identical setup), clearly shows that both components D₁ and D₂ had consistently deepened by about 16% on the second epoch, while their FWHM remained unchanged. The inte-

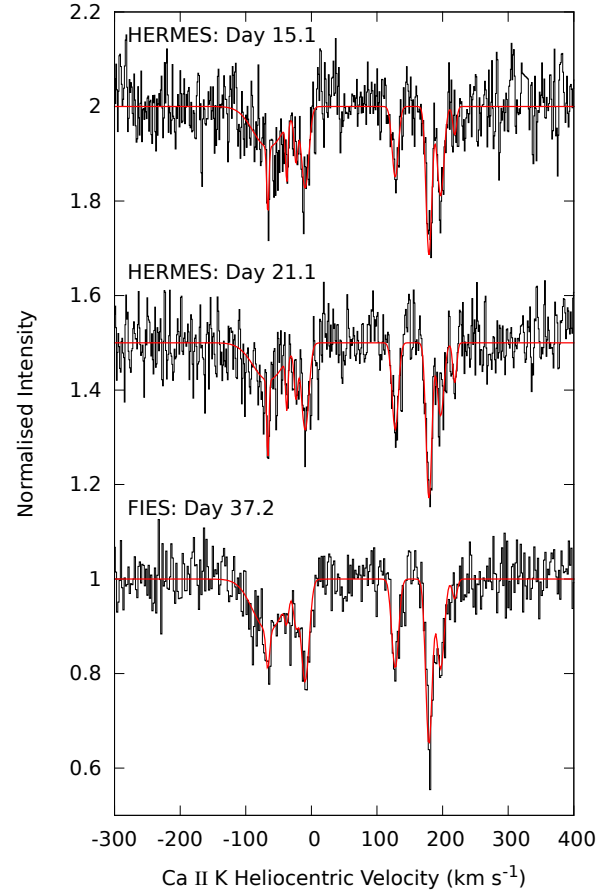


Fig. 4. Ca II K spectra for each epoch for which these data were obtained (black histograms), with best-fit models overlaid (red curves). Spectra have been normalised and offset vertically for display. Heliocentric velocity scale is given with respect to the Ca II K line rest wavelength.

grated EWs directly measured on the two spectra, are 23.6 ± 1.9 , 46.1 ± 2.0 mÅ, and 30.4 ± 2.4 , 53.0 ± 2.5 mÅ for D₁ and D₂ on the two epochs respectively, implying a variation $\Delta EW(\text{Na I D}_2) = 6.9 \pm 3.2$ mÅ. This strengthens the conclusion that whatever the reason for the change is, this cannot be attributed to a variation of instrumental resolution⁴.

A similar check on the EWs can be done using the two SARG observations, which were obtained ~ 75 days apart (see Table 1). The high airmass, and the limited visibility window of SN 2011fe on the second epoch, did not allow us to reach a very high signal-to-noise ratio (~ 16 at 5900Å), so that the EW estimate is rather uncertain. However, the difference is $\Delta EW(\text{Na I D}_2) = 13.3 \pm 6.4$ mÅ, which confirms the variation at the $\sim 2\text{-}\sigma$ level.

Although AES spectra have a significantly lower resolution (16.7 km s⁻¹, see Table 2), given the simple structure of the component at ~ 180 km s⁻¹, they can be used together with the

⁴ Being a fiber-fed spectrograph, FIES is not subject to changes of resolution due to seeing variations. Also, a check on the comparison lamp emission lines on the two epochs shows that the resolution indeed remained constant.

Table 4. Na I D equivalent widths

Setup	Epoch (days)	EW(D ₂) (mÅ)	EW(D ₁) (mÅ)	S/N (5900Å)	Resolution (km s ⁻¹)
(*)	1.5	45.0±9.0	-	-	6.0
FIES#1	8.2	46.1±2.0	23.6±1.9	60	6.3
SARG#1	11.2	46.6±1.5	26.3±1.0	115	4.5
HERMES#1	15.1	44.3±1.8	27.6±1.8	50	3.7
AES#1	21.1	49.2±2.2	34.2±1.9	130	16.7
HERMES#2	21.1	44.3±1.8	27.6±1.8	50	3.7
AES#2	22.1	53.8±4.2	28.5±4.0	105	16.7
AES#3	29.1	51.9±2.7	31.0±2.2	190	16.7
AES#4	30.1	44.5±2.3	33.7±2.5	155	16.7
FIES#2	37.2	53.0±2.5	30.4±2.4	55	6.3
AES#5	56.1	48.7±7.1	34.4±7.3	50	16.7
AES#6+#7	85.2	58.7±3.7	33.5±3.0	115	16.7
SARG#2	86.4	59.9±6.2	23.7±7.3	16	4.5
Weighted average		47.1±0.8	27.4±1.1		

(*)The first epoch is from Nugent et al. (2011c).

higher resolution data to study the variability on the whole time range spanned by the available observations. To increase the signal-to-noise ratio we stacked the last two AES epochs (days 84 and 86).

In Table 4 we report the EWs of Na I D₂ and D₁ directly measured on all our spectra, together with their associated RMS uncertainties, the signal-to-noise ratio achieved at 5900 Å, and the FWHM resolution. The weighted average EWs computed over all epochs for the two lines are 47.1±0.8 mÅ and 27.4±1.1 mÅ, respectively (the standard deviation of the EW measurements is 2.6 and 3.4 mÅ, respectively). The EWs are plotted as a function of time in Fig. 5. Although all measurements are within less than 3-σ from the weighted average (and are therefore formally consistent with a null variation), there is a systematic increase in both components. While the statistical significance for the D₁ component is low, the Pearson correlation factor is 0.82 for D₂. A least squares fit to the data gives $EW(\text{Na I D}_2) = 44.6 \pm 1.4 + (0.159 \pm 0.033) t$, where t is the time from explosion expressed in days. The corresponding slope for D₁ is $0.027 \pm 0.045 \text{ mÅ day}^{-1}$, which is statistically compatible with a null variation. However, we notice that in conditions of mild saturation (as is the case here), $EW(D_2)/EW(D_1) \approx 1.9$. Therefore, assuming the measured slope for the D₂ component, the one expected for D₁ is $\approx 0.08 \text{ mÅ day}^{-1}$, which is not incompatible with the low measured value.

Considering the two extreme values (days 15.1 and 86.4), the observed peak-to-peak Na I D₂ EW variation amounts to $15.6 \pm 6.5 \text{ mÅ}$ (considering days 15.1 and 85.2 this is $14.4 \pm 4.1 \text{ mÅ}$, exceeding the 3-σ level). Although statistically significant, this is very small when compared to the variations seen in SN 2006X (Patat et al. 2007a), and SN 2007le (Simon et al. 2009) during the first 3 months of their evolution, which exceeded 100 mÅ ⁵.

⁵ Even larger variations were reported for SN 1999cl (Blondin et al. 2009) and SN 2006dd (Stritzinger et al. 2010), but no high resolution spectroscopy was available in those cases.

6. Implications on ISM small-scale structure

Given the high velocity of the SN ejecta ($>10^4 \text{ km s}^{-1}$), the photosphere of a Type Ia SN expands very rapidly, reaching a radius larger than 100 AU ($\sim 10^{15} \text{ cm}$) at maximum light, i.e. about 20 days after the explosion. Because of this, the light an observer receives from the SN samples different regions of intervening inter-stellar material (ISM) as time goes by. If the ISM is patchy on the scales of a few tens of AUs, and the density fluctuations are large enough, this can translate into variable absorption features. This geometrical effect and its application to the study of ISM small scale structure are presented in Patat et al. (2010), to which we refer the reader for a detailed discussion. If we include the EW measurement published by Nugent et al. (2011c), the available data allow us to apply this method for the first three months of the SN evolution. During this time interval the photospheric radius increased from $\sim 10 \text{ AU}$ to $\sim 350 \text{ AU}$ (the photospheric radius at our first epoch is $\sim 60 \text{ AU}$. See Patat et al. 2010).

From the fact that the Na I changed by $\lesssim 15 \text{ mÅ}$ over three months, we conclude that the intervening material generating the feature at $\sim 180 \text{ km s}^{-1}$ cannot be confined in an isolated, small ($r < 200 \text{ AU}$) cloud. As the simulations show (Patat et al. 2010, their Fig. 3), such small clouds with central column densities of a few 10^{11} cm^{-2} would be easily detected with the time coverage and the EW accuracy characterizing our data set. If we adopt an upper limit of 15 mÅ for the variation of $EW(D_2)$, we conclude that the cloud responsible for the absorption at $\sim 180 \text{ km s}^{-1}$ must have a radius larger than 250 AU. This does not come as a surprise. The existence of small isolated clouds ($r \sim 100 \text{ AU}$, $N(\text{Na I}) \sim 10^{11} - 10^{12} \text{ cm}^{-2}$), in the past largely invoked to explain the observed H I column density fluctuations, is severely questioned in terms of pressure equilibrium arguments, and the yet unknown mechanisms that would produce them (see Heiles 1997 and references therein). It is therefore more physically meaningful to consider a diffuse ISM, with a fractal structure described by a single power law. As it has been shown by Deshpande (2000), this scenario provides a convincing match to the observations down to AU scales.

The high-resolution coverage of SN 2011fe offers a unique opportunity to derive the small scale structure properties of extra-galactic ISM, a task which can be hardly addressed with any other known technique. For this purpose we have computed a series of models along the lines described in Patat et al. (2010), simulating the observations of our data set, to which we have added the very early epoch by Nugent et al. (2011c). The average column density was set to $N(\text{Na I}) = 2.8 \times 10^{11} \text{ cm}^{-2}$ (corresponding to the weighted average $EW(\text{Na I D}_2)$), and the velocity parameter $b = 3.8 \text{ km s}^{-1}$, as deduced from the line profile fittings. For the power-law spectral index we have used the canonical value $\gamma = -2.8$ (Deshpande 2000). Given the stochastic nature of the fractal clouds, we have adopted a statistical approach, in which the time dependence of $EW(\text{Na I D}_2)$ is examined for a large number (5000) of cloud realizations, as a function of the peak-to-peak variation ΔN on the scale of 1000 AU. The simulations show that peak-to-peak variations $\Delta EW \lesssim 15 \text{ mÅ}$ imply $\Delta N \lesssim 4 \times 10^{11} \text{ cm}^{-2}$ ($\Delta N/N \lesssim 1.4$). With this density contrast, maximum epoch-to-epoch varia-

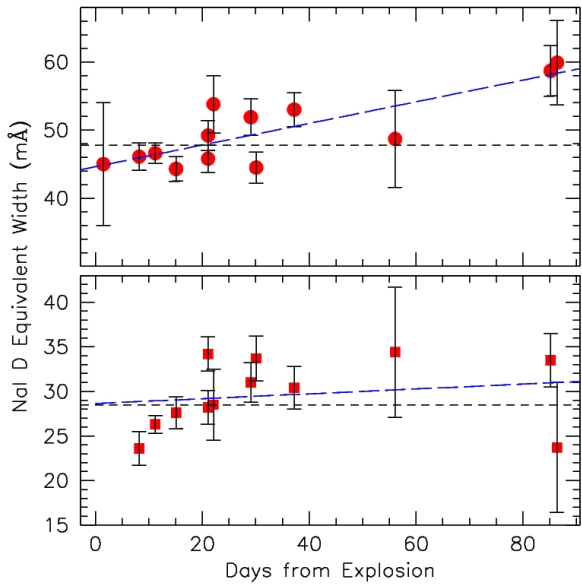


Fig. 5. EW time evolution of Na I D₂ (upper panel) and D₁ (lower panel). Values are from Table 4. The short-dashed horizontal lines mark the weighted average values, whilst the long-dashed lines are least squares fits to the data.

tions reach 9 mÅ between the first (day 1.5) and the second epoch (day 8), with an average absolute variation of ~ 2 mÅ. The maximum epoch-to-epoch variations decrease below ~ 3 mÅ already as of day 11, as the smoothing effect of the extended SN photo-disk grows with time. The maximum deviation measured in our simulations between any pair of epochs in the simulated data-set is ~ 16 mÅ, while the 99-th percentile of the distribution is 12 mÅ. The corresponding average absolute variation is ~ 4 mÅ, with a semi-interquartile range of 2 mÅ. The RMS EW variation from the weighted average is 2.6 mÅ, that matches the value derived from the data (2.7 mÅ, see previous section). The simulated EW(t) curves were analyzed in detail, with the aim of understanding whether the observed time dependency is consistent with the fractal ISM model. They show a smooth behavior, with the EW steadily increasing or decreasing, depending on whether the SN appears projected onto an under- or an over-density region. Slopes $|dEW/dt| \geq 0.1$ mÅ day⁻¹ are observed in $\sim 11\%$ of the cases for $\Delta N/N = 1.4$, while the fraction increases to $\sim 24\%$ for $\Delta N/N = 2$. Therefore, the relatively large slope derived from the observations is somewhat disfavored with respect to milder time dependencies, but still consistent with the adopted model for the ISM structure. For comparison, SN 2007le showed a number of Na I components that remained constant to within a few mÅ for several months (Simon et al. 2009), implying a null variation (i.e. $|dEW/dt| \lesssim 0.03$ mÅ day⁻¹). Our simulations show that for a column density $N(\text{Na I}) = 3 \times 10^{11}$ cm⁻² and $\Delta N/N = 1.4$ this occurs in $\sim 39\%$ of the realizations. For larger fluctuations ($\Delta N/N = 2$) this probability decreases to $\sim 28\%$. Thus, the two different behaviors observed in SNe 2011fe and 2007le are not in contradiction, although the latter is statistically more favored than the former.

The derived density contrast is compatible with the values measured in the Milky Way (Frail et al. 1994) and, therefore, the upper limit on the column density variation is fully in line with what is expected for a diffuse ISM having the same properties as in our own Galaxy. In other words, even in the case the observed fluctuations were real (including the apparent steady growth), these are consistent with the geometrical effect described in Patat et al. (2010). Therefore, we conclude that the absorption feature observed at ~ 180 km s⁻¹ is most likely associated to the ISM, and is placed at distances larger than $\sim 10^{19}$ cm (~ 10 light years) from the explosion site, where the effects of the SN radiation field on the Na I ionization balance are negligible (Patat et al. 2007b; Simon et al. 2009). Unfortunately, the signal-to-noise ratio at ~ 3900 Å in our data is not sufficient to study with the required accuracy the evolution of the Ca II H&K features, which in SNe 2006X and 2007le showed a distinct behavior (Patat et al. 2007a, Simon et al. 2009).

Because of the relatively small distance, it will be possible to follow SN 2011fe with high-resolution spectroscopy as the object fades away. Although this will require larger telescopes, the data may show further variations. As the SN is now entering its nebular phase, it is difficult to make predictions based on our model, because this is based on the presence of a photosphere (Patat et al. 2010). However, as this recedes into the ejecta and the geometry of the emitting material changes with time, it is possible that similar effects take place.

7. Discussion and conclusions

In their analysis, Nugent et al. (2011c) conclude that SN 2011fe is a slightly sub-luminous, Branch-normal explosion, very similar to the well studied SN 1994D (Patat et al. 1996). However, it is by no means clear whether all “normal” events, sharing very similar spectroscopic and photometric properties, do also share a common progenitor channel. For this reason it is important to tie the [reasonably well] known progenitor nature of this particular event to other properties, which may allow us to identify similar events in less favorable cases, i.e. at larger distances and with no such exceptionally early discoveries. Among these is the circumstellar environment.

In the last five years, an alternative way of probing the explosion environment has been deployed. The method and its first application were presented in Patat et al. (2007a), and further expanded in Simon et al. (2009), to which we refer the reader for a more quantitative treatment. The idea is based on the fact that, at variance with core-collapse events, SN Ia are relatively weak UV sources. As a consequence, their ability to ionize possible circumstellar matter is rather limited in distance. Therefore, provided that the gas is placed along the line of sight, it can be revealed by optical absorption lines like Ca II H&K, Na I D, and K I. These are all strong lines, and hence they enable the detection of tiny amounts of material. As opposed to the emission lines that are expected to arise only in the case of direct ejecta-CSM interaction (mainly H and He), absorption lines are generated by material placed virtually at any distance along the line of sight.

This method has now been applied to a number of Type Ia SNe, and in two cases has led to the detection of time-variant Na I features, which were interpreted as arising in the material lost by the progenitor system before the explosion (Patat et al. 2007a; Simon et al. 2009). The velocities of this material are consistent with those of a red giant, hence favoring a symbiotic system. The complex velocity structure shown by SN 2006X was explained as being the possible outcome of recurrent-novae episodes (Patat et al. 2007a). This suggestion is supported by the results of a similar analysis carried out on the known recurrent nova RS Oph, which shows strikingly similar CSM properties (Patat et al. 2011). A study conducted on a large number of SN Ia has shown a statistically significant excess of blue-shifted Na I features, which were interpreted as arising in material lost by the progenitor system (Sternberg et al. 2011). This has given support to the conclusions reached for SNe 2006X and 2007le, which have been suggested to be connected to binary systems hosting a mass-losing giant. If this interpretation is correct, the measured fraction of SN Ia displaying blue-shifted features suggests this channel is not a negligible contributor to the global rate of thermonuclear events. This conclusion is apparently inconsistent with the limits set by the lack of ejecta-wind signatures, and the failed detection of interaction between the ejecta and the companion atmosphere during the very early epochs. Which may simply mean that the picture is not complete yet; see for instance the discussion in Chomiuk et al. (2011) about our understanding of the wind geometry in SN Ia progenitors (see also Patat 2011).

What makes SN 2011fe special is that the progenitor system has been identified with a significant confidence through a number of very stringent constraints (Li et al. 2011; Brown et al. 2011; Nugent et al. 2011c; Bloom et al. 2011; Liu et al. 2011; Horesh et al. 2011). These constraints clearly rule out symbiotic systems with a red giant companion, hence excluding recurrent novae like RS Oph. At least for this one event.

The absence of time-variant, blue-shifted features and the “clean” environment reported in this paper is fully in line with the progenitor nature derived from the very early observations. The bulk of the material transferred from the companion remains confined to within the binary system, and there are no recurrent outbursts that would create the complex CSM structure seen in RS Oph (Patat et al. 2011), and possibly present in SN 2006X (Patat et al. 2007a) and in a significant fraction of other SN Ia ($\geq 20\%$; Sternberg et al. 2011). The key question is whether the argument can be reversed, and the absence of such features in any SN Ia can be interpreted in terms of a similar progenitor, at least in a statistical sense. The answer to this question is awaiting detailed hydrodynamical modeling, which would tell us how frequently the physical conditions for producing observable narrow features are met, and what the viewing angle effects are (Mohamed et al., in preparation). Before this is accomplished, we can only speculate based on very small numbers.

As pointed out by Nugent et al. (2011c), SN 2011fe is spectroscopically very similar to the somewhat sub-luminous events SN 1992A (Kirshner et al. 1993) and SN 1994D (Patat et al. 1996). Although the link between these objects needs to be assessed considering a number of observables, here we can-

not refrain from noticing that all three objects present a very “clean” circum/inter-stellar environment. To illustrate this fact, in Fig. 6 we compare the high-resolution spectra of SN 1994D and SN 2011fe in the velocity ranges corresponding to the host galaxies recession (no measurable absorption features were reported for SN 1992A; Kirshner et al. 1993). Although for SN 1994D there is no time coverage (see also King et al. 1995), the two spectra are remarkably similar.

In the schema devised by Sternberg et al. (2011), SNe 1994D and 2011fe would be classified in the single/symmetric group (SS-type, 14.3%), while SN 1992A would fall in the group with no absorption detection (N-type, 37.1%). An inspection of the SS group shows that 3 SS-type events (out of 5) have a single component, similar to SN 2011fe. If we assume that in all these cases the absorption is attributable to the host galaxy (and not to the CSM environment), and we add them to the N-type events, then the fraction of “clean events” in the Sternberg et al. sample is $\sim 46\%$. One can imagine cases where the CSM environment is “clean”, but the line of sight intercepts ISM clouds that are totally unrelated to the progenitor. Therefore, while the lack of conspicuous absorption features can be confidently interpreted in terms of a gas-free environment, the reverse argument does not hold.

The projected position of SN 2011fe falls close to a peripheral spiral arm (see for instance Nugent et al. 2011c). However, the very low reddening and the absence of complex absorption structures strongly suggest the explosion took place on the front side of the face-on host, most probably well above its galactic plane. Had the SN been placed on the rear side of the galaxy, the IS imprints would have been much more complex, irrespective of the progenitor’s nature deduced from the early data. Therefore the above fraction can only represent a lower limit. On the other hand, because of the viewing angle effects, the fraction of events allegedly produced by systems hosting a giant estimated by Sternberg et al. (2011) is also a lower limit (20-25%).

The sample of SN Ia with sufficient spectral resolution and time coverage is still relatively small, and therefore drawing conclusions may be premature. The fraction of events showing time-variant features is $\sim 17\%$ (Patat 2011). Probing only the line of sight, this indicator also suffers from viewing angle effects. In addition, the method only reveals material placed in the suitable range of distances from the SN, and having the required densities (Patat et al. 2007a; Simon et al. 2009). Therefore, again, it gives only a lower limit to the fraction of events generated through this channel. Interestingly, this limit is reasonably similar to that derived from the excess of blue-shifted features (20%; Sternberg et al. 2011), and it confirms the conclusion that this channel contributes in a significant way to the global SN Ia rate. This result has still to come to terms with the opposite evidences given by the lack of CSM signatures in radio, UV, and X-rays domains, and the failed detection of extended companion atmospheres in the early stages of the SN evolution.

Although expensive in terms of telescope time, multi-epoch, high-resolution spectroscopy of SN Ia constitutes a powerful and independent tool for investigating the nature of SN Ia progenitors. With the future availability of statistically

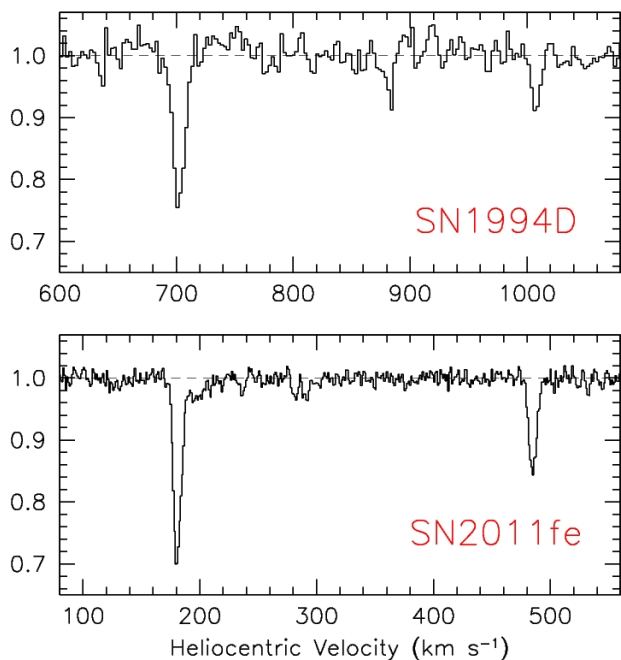


Fig. 6. Comparison between the Na I D spectral regions of SN 1994D (upper; Patat et al. 1996), and SN 2011fe (lower; SARG). Heliocentric velocities are computed with respect to the D₂ component. The resolution of the SN 1994D spectrum is $\sim 10 \text{ km s}^{-1}$.

significant samples, it will most likely help us in settling the matter about the contribution of the various channels leading to Type Ia explosions. And all the pieces that currently appear to form a contradictory set of information may fall together to form a consistent picture.

Acknowledgements. This work has been conducted in the framework of the European collaboration SN Variety and Nucleosynthesis Yields.

This work is partially based on observations made with the Mercator Telescope, operated on the island of La Palma by the Flemish Community, at the Spanish Observatorio del Roque de los Muchachos of the Instituto de Astrofísica de Canarias.

This work is partially based on observations obtained with the HERMES spectrograph, which is supported by the Fund for Scientific Research of Flanders (FWO), Belgium, the Research Council of K.U.Leuven, Belgium, the Fonds National Recherches Scientific (FNRS), Belgium, the Royal Observatory of Belgium, the Observatoire de Geneve, Switzerland and the Thüringer Landessternwarte Tautenburg, Germany.

This work is partially based on observations made with the Nordic Optical Telescope, operated on the island of La Palma jointly by Denmark, Finland, Iceland, Norway, and Sweden, in the Spanish Observatorio del Roque de los Muchachos of the Instituto de Astrofísica de Canarias.

This work is partially based on observations made with the SARG spectrograph at the Italian Telescopio Nazionale Galileo (TNG), operated on the island of La Palma by the Fundación Galileo Galilei of the INAF (Istituto Nazionale di Astrofisica) at the Spanish Observatorio del Roque de los Muchachos of the Instituto de Astrofísica de Canarias.

This work is partially based on data collected at the 1.82 m Copernico telescope on Mt. Ekar (Asiago, Italy).

M. C. thanks the NASA Astrobiology Institute via the Goddard Center for Astrobiology.

V.S. acknowledges financial support from Fundação para a Ciência e a Tecnologia under program Ciência 2008 and a research grant PTDC/CTE-AST/112582/2009.

References

- Bertin, P., Lallement, R., Ferlet, R. & Vidal-Madjar, A., 1993, *A&A*, 278, 549
- Bianco, F. B., et al., 2011, *ApJ*, 741, 20
- Blondin, S., et al., 2009, *ApJ*, 693, 207
- Bloom, J. S., et al., 2011, *ApJ* submitted (arXiv:1111.0966v1)
- Bosma, A., Goss, W. M. & Allen, R. J., 1981, *A&A*, 93, 106
- Brown, P. J., et al., 2011, *ApJ* submitted (arXiv:1110.2538v1)
- Chomiuk, L., Soderberg, A.M., Chevalier, R., Badenes, C. & Fransson, C. 2011, *AAS*, 21730405C
- Clough, S. A., Shephard, M. W., Mlawer, E. K. et al., 2005, *J. Quant. Spectrosc. Radiat. Transfer*, 91, 233
- Cox, N. L. J., et al., 2007, *A&A*, 470, 941
- Cox, N. L. J. & Patat, F., *A&A*, 485, L9
- Crawford, I. A., 1992, *MNRAS*, 254, 264
- de Vaucouleurs, G., de Vaucouleurs, A., Corwin, H. G., Buta, R. J., Paturel, G., & Fouqué, P., 1991, *Third Reference Catalogue of Bright Galaxies*, Ver. 3.9
- Deshpande, 2000, *MNRAS*, 317, 199
- Frail, D. A., Weisberg, J. M., Cordes, H. M., & Mathers, A., 1994, *ApJ*, 436, 144
- Gratton, R. G., Bonanno, G., Bruno, P., et al. 2001, *Experimental Astronomy*, 12, 107
- Hayden, B. T., et al., 2010, *ApJ*, 722, 1691
- Heiles, C., 1997, *ApJ*, 481, 193
- Herbig, G. H., 1995, *ARA&A*, 33, 19
- Hobbs, L. M., 1978, *ApJS*, 38, 129
- Horesh, A., et al., 2011, *ApJ*, submitted, (arXiv:1109.2912v1)
- Horne, K., 1986, *PASP*, 98, 609
- Howarth, I. D., Price, R. J., Crawford, I. A. & Hawkins, I., 2002, *MNRAS*, 335, 267
- Immler, S. I. et al. 2006, *ApJ*, 648, L119
- Kasen, D., 2010, *ApJ*, 708, 1025
- King, D. L., et al., 1995, *A&A*, 300, 881
- Kirshner, R. P., et al., 1993, *ApJ*, 415, 589
- Leonard, D.C. 2007, *ApJ*, 670, 1275
- Li, W., et al., 2001, *Nature*, submitted (arXiv:1109.1593)
- Liu, J., Di Stefano, R., Wang, T., & Moe, M., *ApJL* submitted (arXiv:1110.2506v1)
- Luna, R., et al., 2008, *A&A*, 480, 133
- Lundqvist, P. et al. 2003, in *From twilight to highlight: the physics of Supernovae*, ed. W. Hillebrandt & B. Leibundgut (Berlin: Springer), 309
- Lundqvist, P. et al. 2005, in *Cosmic Explosions*, ed. J. M. Marcaide, & K. W. Weiler, CD-ROM version, IAU Coll., 192, 81
- Marietta, E., Burrows, A. & Fryxell, B. 2000, *ApJ*, 128, 615
- Mattila, S. et al. 2005, *A&A*, 443, 649
- Molaro, P., et al., 1993, *A&A*, 274, 505
- Munari, U. & Zwitter, U., 1997, *A&A*, 318, 269
- Nugent, P., et al., 2011a, *ATel* #3581
- Nugent, P., et al., 2011b, *CBET*, 2791, 1
- Nugent, P. E., et al., 2011c, *Nature*, in press (arXiv:1110.6201v1)
- Panagia, N., et al. 2006, *ApJ*, 469, 396
- Patat, F., et al., 1996, *MNRAS*, 278, 111
- Patat, F., et al., 2007a, *Science*, 30, 490
- Patat, F., et al., 2007b, *A&A*, 474, 931

- Patat, F., Cox, N. L. J., Parrent, J., & Branch, D., 2010, *A&A*, 514, 78
- Patat, F., Chugai, N. N., Podsiadlowski, Ph., Mason, E., Melo, C. & Pasquini, L., 2011, *A&A*, 530, 63
- Patat, F., 2011, in "Binary paths to Type Ia Supernova explosions", IAU S. 281, AIPC, R. Di Stefano & M. Orlo eds., in press (arXiv:1109.5799)
- Raskin, G., et al., 2011, *A&A*, 526A, 69
- Schlegel, D. J., Finkbeiner, D. P. & Davis, M., 1998, *ApJ*, 500, 525
- Rothman, L.S., et al., 2009, *J. Quant. Spectrosc. Radiat. Transfer*, 110, 533
- Seifahrt, A., Käufel, H. U., Zängl, G., Bean, J. L., Richter, M. J. & Siebenmorgen, R., 2010, *A&A*, 524A, 11
- Sembach, K. R. & Danks, A. C., 1994, *A&A*, 289, 539
- Siluk, R. S., & Silk, J., 1974, *ApJ*, 192, 51
- Simon, J., et al., 2009, *ApJ*, 702, 1157
- Sollerman, J., et al., 2005, *A&A*, 429, 559
- Sternberg, A., et al., 2011, *Science*, 333, 856
- Stevenson, C.C., 1994, *MNRAS*, 267, 904
- Stritzinger, M., et al., 2010, *AJ*, 140, 2036
- Whelan, J. & Iben, I., 1973, *ApJ*, 186, 1007